Passive Material Properties of Intact Ventricular Myocardium Determined From a Cylindrical Model

J. M. Guccione

A. D. McCulloch
Assoc. Mem. ASME.
Department of Applied Mechanics and
Engineering Sciences (Bioengineering),

L. K. Waldman
Department of Medicine (Cardiology),
The University of California, San Diego,
La Jolla, Calif. 92093-0412

The equatorial region of the canine left ventricle was modeled as a thick-walled cylinder consisting of an incompressible hyperelastic material with homogeneous exponential properties. The anisotropic properties of the passive myocardium were assumed to be locally transversely isotropic with respect to a fiber axis whose orientation varied linearly across the wall. Simultaneous inflation, extension, and torsion were applied to the cylinder to produce epicardial strains that were measured previously in the potassium-arrested dog heart. Residual stress in the unloaded state was included by considering the stress-free configuration to be a warped cylindrical arc. In the special case of isotropic material properties, torsion and residual stress both significantly reduced the high circumferential stress peaks predicted at the endocardium by previous models. However, a resultant axial force and moment were necessary to cause the observed epicardial deformations. Therefore, the anisotropic material parameters were found that minimized these resultants and allowed the prescribed displacements to occur subject to the known ventricular pressure loads. The global minimum solution of this parameter optimization problem indicated that the stiffness of passive myocardium (defined for a 20 percent equibiaxial extension) would be 2.4 to 6.6 times greater in the fiber direction than in the transverse plane for a broad range of assumed fiber angle distributions and residual stresses. This agrees with the results of biaxial tissue testing. The predicted transmural distributions of fiber stress were relatively flat with slight peaks in the subepicardium, and the fiber strain profiles agreed closely with experimentally observed sarcomere length distributions. The results indicate that torsion, residual stress and material anisotropy associated with the fiber architecture all can act to reduce endocardial stress gradients in the passive left ventricle.

Introduction

Although global measures of ventricular function such as blood pressure, its derivatives with respect to time and ventricular volume, and ejection fractions have been useful for assessing total cardiac performance, an understanding of regional ventricular function requires accurate estimates of myocardial stresses and strains, and hence the material properties of intact myocardium. There are many reasons for studying the mechanics of the intact myocardium: (1) ventricular wall stress is a primary determinant of myocardial oxygen consumption [1] and coronary blood flow [2]; (2) accurate distributions of ventricular stress and strain are required to interpret the localized contractile disorders caused by myocardial ischemia [3,4] and infarct [5,6]; (3) changes in wall stress may influence growth and hypertrophy of intact cardiac muscle [7,8]; (4) understanding the microanatomical and ultrastructural basis of cardiac function requires knowledge of the material properties of intact myocardium in health and disease [9].

The most significant problem in modeling the mechanics of the passive left ventricle is the absence of a three-dimensional constitutive equation for stress in the passive myocardium. Because isolated papillary muscle and trabeculae preparations only permit one-dimensional stress-strain measurements, investigators have begun performing biaxial tests using isolated sheets of ventricular myocardium [10]. However, there are potential difficulties with these measurements largely associated with contracture and the unknown effects of resecting sections of ventricular wall. Although Yin and co-workers [10] have concluded from biaxial measurements in isolated left ventricular myocardium that passive cardiac muscle is anisotropic, their findings were too variable to establish whether—under the loading conditions present in the intact ventricular wall—the muscle is stiffer in the fiber or cross-fiber direction. Nevertheless, biaxial testing does confirm that passive myocardium exhibits the exponential stress-strain relationship, an-
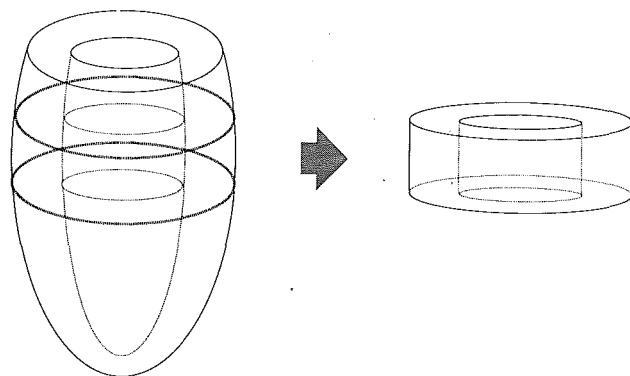
Fig. 1   The geometry of the left ventricular equatorial region approximated by a cylinder

LV Residual Stresses Relieved   Unloaded Passive LV   Loaded End-Diastolic LV
('Stress-Free' Reference State)   (Strain reference state)   (Inflated, stretched and twisted)

Fig. 2   Passive left ventricular deformation modeled by flexure, followed by inflation, stretch and twist of the cylinder

isotropy, and strain-rate-independent hysteresis characteristic of soft biological tissues [11]. However, the main problem with existing experimental tests of isolated tissues is uncertainty about how well they describe the properties of the *intact* ventricular muscle.

Therefore, in this paper we propose a model that provides an approach to quantifying the material properties of intact myocardium that complements biaxial testing. A thick-walled cylindrical geometry is used to represent the equatorial region of the passive left ventricle. Based on the results of uniaxial and biaxial tests in isolated cardiac muscle [10,11], the myocardium is assumed to be a transversely isotropic material with preferred directions that vary transmurally. Changes in these axes of material symmetry are chosen to correspond with fiber orientations that have been observed to vary continuously across the wall thickness in the dog and other mammals. The myocardium is modeled as a homogeneous hyperelastic material that is incompressible. The stress-free state of the left ventricle is assumed to be a warped cylindrical arc based on experimental measurements of the stress-free shape of the potassium-arrested rat heart [12] due to the absence of these data for the dog. To model the effects of passive pressure loading, finite deformations are prescribed that give rise to epicardial strains measured previously at the midanterior free wall of the isolated arrested canine heart [13].

Concomitant with the prescribed deformations, which include inflation, stretch and torsion of the cylinder, resultant forces and moments exist [14–17] with magnitudes depending on the chosen material parameters. The only applied force in the isolated heart is the pressure in the left ventricular cavity. Thus, to determine the material properties of the intact myocardium, the parameters of the constitutive law are optimized while the model is constrained both to satisfy the known stress boundary conditions and to undergo the experimentally measured displacements. In addition, the significance of the model assumptions are examined by altering, independently, the parameters that describe the kinematics, fiber orientations and material properties of the model. The results of the analysis may provide more realistic estimates of myocardial material properties and the transmural distributions of stresses and strains.

Methods

Using the theory of large elastic deformations, a general type of axisymmetric deformation was applied to a cylindrical body to model the transmural finite strain distribution in an equatorial region of the passive left ventricular free wall. The general form of the cylinder problem in finite elasticity was given by Adkins [18], who solved the equilibrium equations for several special cases in which the coordinates that defined the curvilinear aeolotropy of the material coincided with the reference cylindrical polar coordinates. Here, we consider the
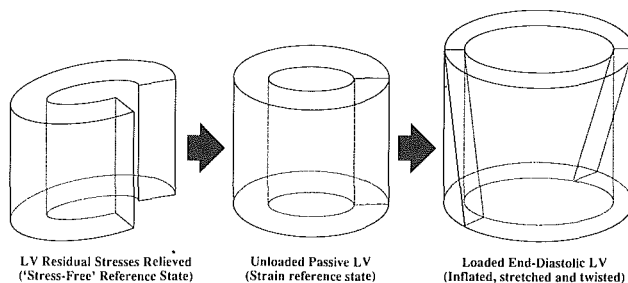
case in which the material is aeolotropic with respect to a fiber axis field where the fiber angle varies linearly through the wall. Nonlinear elastic material properties were defined by an exponential strain-energy function of Lagrangian strain components referred to a locally orthonormal coordinate system with one axis aligned with the muscle fibers. To clarify the role of residual stress and strain, displacements are prescribed in two steps [19]. First, the cylindrical arc is deformed from the stress-free state to the intact unloaded configuration. Then, displacements are prescribed to model the deformation of the cylinder during passive loading.

Kinematics. The geometry of the left ventricle in the unloaded and loaded states was approximated by a thick-walled, circular cylindrical tube (Fig. 1). Rather than assuming that the left ventricle is stress-free in the unloaded (zero transmural pressure) configuration, it is assumed that residual stress is relieved by making a single radial cut in the unloaded ventricular wall so that a circumferential ring of the left ventricle springs open into a cylindrical arc as observed by Omens and Fung [12]. In general, the circumferential ring may not remain planar after the radial cut, and its axial thickness may change. Therefore, a sector of a hollow cylinder (Fig. 2) that may be stretched and 'warped' to form part of a left-handed helix defined the stress-free body. To determine the 'residual' strain in the unloaded state, this sector was deformed back into a closed tube. In addition to circumferential and longitudinal extensions, torsional shears have been observed in the passive heart [13]. Although they have not yet been measured experimentally in the passive heart, transverse shears also exist in the beating heart [20]. Hence, a cylindrically symmetric deformation (inflation, stretch, torsion, azimuthal and axial shear) was prescribed then to simulate the effects of passive pressure loading [17,18].

First, consider a warped sector of a cylinder of length Z_2 that is bounded in the cylindrical polar reference coordinate system (R, Θ, Z) by curved surfaces $R = R_1$ and $R = R_2$ and the planes $\Theta = 0$ and $\Theta = \Theta_2$. The slope of the partial helix is $-\gamma_1$. The following displacements deform this sector into a simple cylindrical tube:

(i)   a uniform simple warping shear in which planes perpendicular to the circumference of the initially warped sector are displaced axially so that the warping is removed and the sector is bounded by the planes $Z = 0$ and $Z = Z_2$;

(ii)   a uniform circumferential flexion sufficient to make the cut edges meet. The circumferential extension ratio α is related to Θ_2 by $\alpha_1 = 2\pi/\Theta_2$;

(iii)   a corresponding uniform radial deflation of the tube in which the deformed internal and external radii become ρ_1 and ρ_2, respectively;

(iv)   a simple extension of extension ratio ϵ_1, parallel to the axis of the cylinder, so that its length becomes $\epsilon_1 Z_2$.

The unloaded, but not stress-free, body is bounded by the coordinate surfaces $\rho_1 \leq \rho \leq \rho_2$, $0 < \varphi < 2\pi$, and $0 < \zeta < \zeta_2$, where (ρ, φ, ζ) are cylindrical polar coordinates and the deformation is given by Adkins [18]

$$\rho = \rho(R), \quad \varphi = \alpha_1 \Theta, \quad \text{and} \quad \zeta = \gamma_1 \Theta + \epsilon_1 Z. \tag{1a}$$

Then the unloaded configuration is subjected to the following deformations to simulate passive filling:

(i) a uniform radial inflation of the tube in which the deformed internal and external radii become r_1 and r_2, respectively;

(ii) a uniform simple torsion in which planes perpendicular to the axis of the tube are rotated about that axis through an angle proportional to the undeformed axial coordinate, the constant of proportionality being β_2;

(iii) a simple extension of extension ratio ϵ_2, parallel to the axis of the cylinder, so that its length becomes ϵZ_2, where $\epsilon = \epsilon_1 \epsilon_2$;

(iv) an azimuthal shear of the tube, in which each point moves about the longitudinal axis through an angle ϕ, which is a function only of the radius at the point;

(v) an axial shear of the tube, in which each point moves parallel to the axis of the tube through a distance ω, which is a function of the radius alone.

The loaded body is bounded by the coordinate surfaces $r_1 \leq r \leq r_2, 0 < \theta < 2\pi$, and $0 < z < z_2$, where (r, θ, z) are cylindrical polar coordinates and the deformation from the unloaded configuration to the loaded state is given by

$$r = r(\rho), \quad \theta = \phi(\rho) + \varphi + \beta_2 \zeta, \quad \text{and} \quad z = \omega(\rho) + \epsilon_2 \zeta. \tag{1b}$$

From equation (1a), the deformation gradient tensor F_1 is obtained with the following matrix of components in cylindrical polar coordinates (see Spencer [21], p. 158):

$$\mathbf{F}_1 = \begin{bmatrix} \dfrac{\partial \rho}{\partial R} & \dfrac{1}{R}\dfrac{\partial \rho}{\partial \Theta} & \dfrac{\partial \rho}{\partial Z} \\[2mm] \rho\dfrac{\partial \varphi}{\partial R} & \dfrac{\rho}{R}\dfrac{\partial \varphi}{\partial \Theta} & \rho\dfrac{\partial \varphi}{\partial Z} \\[2mm] \dfrac{\partial \zeta}{\partial R} & \dfrac{1}{R}\dfrac{\partial \zeta}{\partial \Theta} & \dfrac{\partial \zeta}{\partial Z} \end{bmatrix} = \begin{bmatrix} \dfrac{d\rho}{dR} & 0 & 0 \\[2mm] 0 & \dfrac{\alpha_1 \rho}{R} & 0 \\[2mm] 0 & \dfrac{\gamma_1}{R} & \epsilon_1 \end{bmatrix}. \tag{2a}$$

Similarly, from equation (1b), the deformation gradient tensor F_2 is obtained with the following matrix of components in cylindrical polar coordinates:

$$\mathbf{F}_2 = \begin{bmatrix} \dfrac{\partial r}{\partial \rho} & \dfrac{1}{\rho}\dfrac{\partial r}{\partial \varphi} & \dfrac{\partial r}{\partial \zeta} \\[2mm] r\dfrac{\partial \theta}{\partial \rho} & \dfrac{r}{\rho}\dfrac{\partial \theta}{\partial \varphi} & r\dfrac{\partial \theta}{\partial \zeta} \\[2mm] \dfrac{\partial z}{\partial \rho} & \dfrac{1}{\rho}\dfrac{\partial z}{\partial \varphi} & \dfrac{\partial z}{\partial \zeta} \end{bmatrix} = \begin{bmatrix} \dfrac{dr}{d\rho} & 0 & 0 \\[2mm] r\dfrac{d\phi}{d\rho} & \dfrac{r}{\rho} & \beta_2 r \\[2mm] \dfrac{d\omega}{d\rho} & 0 & \epsilon_2 \end{bmatrix}. \tag{2b}$$

Finally, from equations (2a) and (2b), one obtains the deformation gradient tensor for the combined deformation $F = F_2 \cdot F_1$ having the following components in cylindrical polar coordinates:

$$(F_{iS}) = \begin{bmatrix} \dfrac{\partial r}{\partial R} & \dfrac{1}{R}\dfrac{\partial r}{\partial \Theta} & \dfrac{\partial r}{\partial Z} \\[2mm] r\dfrac{\partial \theta}{\partial R} & \dfrac{r}{R}\dfrac{\partial \theta}{\partial \Theta} & r\dfrac{\partial \theta}{\partial Z} \\[2mm] \dfrac{\partial z}{\partial R} & \dfrac{1}{R}\dfrac{\partial z}{\partial \Theta} & \dfrac{\partial z}{\partial Z} \end{bmatrix} = \begin{bmatrix} \dfrac{dr}{dR} & 0 & 0 \\[2mm] r\dfrac{d\phi}{dR} & \dfrac{\alpha r}{R} & \beta r \\[2mm] \dfrac{d\omega}{dR} & \dfrac{\gamma}{R} & \epsilon \end{bmatrix}, \tag{2c}$$

where $\alpha = \alpha_1 + \beta_2 \gamma_1$, $\beta = \beta_2 \epsilon_1$ and $\gamma = \gamma_1 \epsilon_2$. The constants α and ϵ are the extension ratios in the circumferential and axial directions, respectively. The constant β is the twist per unit undeformed length, and γ is the axial displacement per radian undeformed circumference. ϕ and ω are angular and axial displacements, respectively, which are functions of R alone. The functions $r(R)$, $\phi(R)$, and $\omega(R)$ depend on the material

properties of the model. The deformed radius $r(R)$ is determined by the kinematic incompressibility constraint. The circumferential and axial equations of equilibrium must be solved to find $\partial \phi / \partial r$ and $\partial \omega / \partial R$.

From the kinematic incompressibility constraint that the third principal invariant of strain I_3 is unity, one has

$$I_3 = (\det F)^2 = \left(\frac{\lambda r}{R}\frac{dr}{dR}\right)^2 = 1 \quad \text{or} \quad \frac{dr}{dR} = \frac{R}{\lambda r}, \tag{3}$$

in which $\lambda = \alpha \epsilon - \beta \gamma$. Integrating equation (3) gives

$$r(R) = \sqrt{\frac{R^2 - R_1^2}{\lambda} + r_1^2}. \tag{4}$$

The Lagrangian Green's strain tensor E is defined by

$$E = \frac{1}{2}(F^{\mathrm{T}} \cdot F - I), \tag{5}$$

where I is the identity tensor. Hence from equations (2), (3), and (5), the components of E, with respect to cylindrical polar coordinates, are:

$$E_{RR} = \frac{1}{2}\left[\left(\frac{R}{\lambda r}\right)^2 + \left(r\frac{d\phi}{dR}\right)^2 + \left(\frac{d\omega}{dR}\right)^2 - 1 \right], \tag{6a}$$

$$E_{\Theta\Theta} = \frac{1}{2}\left[\left(\frac{\alpha r}{R}\right)^2 + \left(\frac{\gamma}{R}\right)^2 - 1 \right], \tag{6b}$$

$$E_{ZZ} = \frac{1}{2}(\beta^2 r^2 + \epsilon^2 - 1), \tag{6c}$$

$$E_{R\Theta} = \frac{1}{2}\left(\frac{\alpha r^2}{R}\frac{d\phi}{dR} + \frac{\gamma}{R}\frac{d\omega}{dR} \right), \tag{6d}$$

$$E_{\Theta Z} = \frac{1}{2}\left(\frac{\alpha \beta r^2}{R} + \frac{\gamma \epsilon}{R} \right), \tag{6e}$$

$$E_{ZR} = \frac{1}{2}\left(\beta r^2 \frac{d\phi}{dR} + \epsilon \frac{d\omega}{dR} \right). \tag{6f}$$

Stress-Strain Relations. Passive myocardium was modeled as a homogeneous incompressible hyperelastic material possessing curvilinear aeolotropy with respect to the local muscle fiber axis. The assumption of incompressibility has been found to be justified for unperfused myocardium [22]. The helical fibrous structure of the left ventricle was represented by a system of curvilinear material coordinates (X_R, X_F, X_C) which were orthogonal in the stress-free state. The fiber axis X_F lies in the plane of the wall normal to the radial axis. X_C is the cross-fiber in-plane axis, and X_R coincides with R. The fiber angle Ψ, which was referred to the circumferential direction, was constant in the axial and circumferential directions, and its transmural variation was continuous and linear

$$\Psi(R) = \Psi_1 \left(\frac{R_2 - R}{R_2 - R_1}\right) + \Psi_2 \left(\frac{R - R_1}{R_2 - R_1}\right), \tag{7}$$

where Ψ_1 and Ψ_2 are the endocardial and epicardial fiber angles, respectively.

The components E_{LM} of the strain tensor (equation (6)) in cylindrical polar coordinates (R, Θ, Z) were transformed to fiber coordinates (X_R, X_F, X_C) by a rotation matrix Q which rotates a vector in the plane of the wall $(R = \text{constant})$ through the angle $\Psi(R)$ about the radial axis. Hence, the matrix $\overline{E}$ of strain components referred to fiber coordinates is given by

$$\overline{E} = QEQ^{\mathrm{T}}, \tag{8}$$

where

$$\mathbf{Q} = \begin{bmatrix} 1 & 0 & 0 \\ 0 & \cos\Psi(R) & \sin\Psi(R) \\ 0 & -\sin\Psi(R) & \cos\Psi(R) \end{bmatrix}.$$

The general form of the constitutive equation for a hyperelastic solid (see Spencer [21], p. 138) may be expressed in terms of the strains by an elastic potential function W^*

$$T_{ij} = \frac{\sqrt{I_3}}{2} F_{iS} F_{jT} \left(\frac{\partial W^*}{\partial E_{ST}} + \frac{\partial W^*}{\partial E_{TS}} \right) \qquad (9)$$

For an incompressible material I_3 must equal 1, and the hydrostatic pressure variable p enters the constitutive equation as a Lagrange multiplier:

$$W^* = W(E_{ST}) - \frac{1}{2} p(I_3 - 1).$$

Hence,

$$T_{ij} = \frac{1}{2} F_{iS} F_{jT} \left(\frac{\partial W}{\partial E_{ST}} + \frac{\partial W}{\partial E_{TS}} \right) - p\delta_{ij}, \qquad (10)$$

where T_{ij} are components of the Cauchy stress tensor T referred to cylindrical polar coordinates (r, θ, z) in the deformed body, W is the strain-energy function, p is determined from the equations of equilibrium and boundary conditions, and δ_{ij} is the Kronecker delta. If W is a function of fiber strain components $\overline{\mathbf{E}}$, then

$$\frac{\partial W}{\partial E_{ST}} = \frac{\partial W}{\partial \overline{E}_{LM}} \frac{\partial \overline{E}_{LM}}{\partial E_{ST}} = Q_{LS} Q_{MT} \frac{\partial W}{\partial \overline{E}_{LM}}. \qquad (11)$$

Substituting equation (11) into equation (10) and defining $\mathbf{A} = \mathbf{F}\mathbf{Q}^{\mathrm{T}}$, we have

$$T_{ij} = \frac{1}{2} (A_{iL} A_{jM} + A_{iM} A_{jL}) \frac{\partial W}{\partial \overline{E}_{LM}} - p\delta_{ij}, \qquad (12)$$

where

$$(A_{iL}) = \begin{bmatrix} \dfrac{R}{\lambda r} & 0 & 0 \\[2ex] r\dfrac{d\phi}{dR} & \dfrac{\alpha r}{R}\cos\Psi(R) + \beta r\sin\Psi(R) & -\dfrac{\alpha r}{R}\sin\Psi(R) + \beta r\cos\Psi(R) \\[2ex] \dfrac{d\omega}{dR} & \dfrac{\gamma}{R}\cos\Psi(R) + \epsilon\sin\Psi(R) & -\dfrac{\gamma}{R}\sin\Psi(R) + \epsilon\cos\Psi(R) \end{bmatrix}.$$

Choung and Fung [23] have proposed the following form of strain-energy function to describe the three-dimensional mechanical properties of arteries assuming orthotropic material symmetry:

$$W = \frac{C}{2}(e^Q - 1). \qquad (13)$$

where Q is a quadratic function of the three principal strain components. Using the material symmetry relations given by Green and Adkins [24, p. 25], we chose the following new form for Q to describe the special case of three-dimensional transverse isotropy with respect to the fiber coordinate system:

$$Q = 2b_1(\overline{E}_{RR} + \overline{E}_{FF} + \overline{E}_{CC})$$
$$+ b_2 \overline{E}_{FF}^2 + b_3 (\overline{E}_{CC}^2 + \overline{E}_{RR}^2 + \overline{E}_{CR}^2 + \overline{E}_{RC}^2)$$
$$+ b_4 (\overline{E}_{RF}^2 + \overline{E}_{FR}^2 + \overline{E}_{FC}^2 + \overline{E}_{CF}^2),$$

where C and b_1 to b_4 are absolute constants which are independent of deformation and position in the body. The material constant C simply scales the stresses; however, certain combinations of the coefficients in the exponent Q allow the model

material to possess various material symmetries. When b_1 is the only non-zero coefficient in Q or when $b_2 = b_3 = b_4$, the model material is isotropic. The material stiffness is increased in the fiber or transverse directions by increasing b_2 or b_3, respectively, from zero. The rigidity of the material under shear in the (X_R, X_F) and (X_F, X_C) planes is directly related to b_4. Similarly, b_3 modifies the shearing properties of the model material in the (X_C, X_R) plane. Different combinations of these material parameters were determined from the prescribed displacements and the known stress boundary conditions. Full expressions for the stress components with respect to cylindrical polar coordinates are given in Appendix 1.

A unit vector n in the direction of the deformed fibers is related to the unit vector N in the direction of the undeformed fibers by the equation (see Spencer [21], p. 69)

$$n = \lambda_N^{-1} F \cdot N, \qquad (14)$$

where λ_N is the fiber extension ratio. Denoting by ψ the deformed fiber angle, which is only a function of the deformed radial coordinate r, the components of n and N are

$$n^{\mathrm{T}} = [0 \ \cos\Psi(r) \ \sin\Psi(r)], \quad N^{\mathrm{T}} = [0 \ \cos\Psi(R) \ \sin\Psi(R)]. \qquad (15)$$

Using equations (2), (14), and (15), one may write

$$\begin{bmatrix} 0 \\ \cos\psi(r) \\ \sin\psi(r) \end{bmatrix} = \frac{1}{\lambda_N} \begin{bmatrix} 0 \\ \dfrac{\alpha r}{R}\cos\Psi(R) + \beta r\sin\Psi(R) \\ \dfrac{\gamma}{R}\cos\Psi(R) + \epsilon\sin\Psi(R) \end{bmatrix}, \qquad (16)$$

and therefore,

$$\psi(r) = \tan^{-1} \left[\frac{\dfrac{\gamma}{R}\cos\Psi(R) + \epsilon\sin\Psi(R)}{\dfrac{\alpha r}{R}\cos\Psi(R) + \beta r\sin\Psi(R)} \right]. \qquad (17)$$

By analogy with equation (8), the matrix $\mathbf{T}$ of components of the Cauchy stress tensor in cylindrical polar coordinates are transformed to fiber coordinate components $\overline{\mathbf{T}}$ by the rotation matrix $\mathbf{q}$ (see Appendix 1):

$$\overline{\mathbf{T}} = \mathbf{q}\mathbf{T}\mathbf{q}^{\mathrm{T}}, \qquad (18)$$

where

$$\mathbf{q} = \begin{bmatrix} 1 & 0 & 0 \\ 0 & \cos\psi(r) & \sin\psi(r) \\ 0 & -\sin\psi(r) & \cos\psi(r) \end{bmatrix}.$$

Equilibrium Equations and Boundary Conditions. Neglecting body forces and inertial effects, the equations of equilibrium are (see Spencer [21], p. 160)

$$\mathrm{div}\, T = 0,$$

and noting from equations (A1) that the components of the Cauchy stress tensor in these polar coordinates for this axisymmetric deformation are functions of r alone,

$$\frac{dT_{rr}}{dr} + \frac{T_{rr} - T_{\theta\theta}}{r} = 0, \qquad (19a)$$

$$\frac{dT_{r\theta}}{dr} + \frac{2T_{r\theta}}{r} = 0, \qquad (19b)$$

$$\frac{dT_{rz}}{dr} + \frac{T_{rz}}{r} = 0. \qquad (19c)$$

Integrating equations (19b) and (19c) gives

$$r^2 T_{r\theta} = r_1^2 T_{r\theta}|_{r=r_1} \quad \text{and} \quad rT_{rz} = r_1 T_{rz}|_{r=r_1}, \qquad (20)$$

where $T_{r\theta}|_{r=r_1}$ and $T_{rz}|_{r=r_1}$ are the shear stresses acting on the inner surface in the circumferential and axial directions, respectively. Since $T_{rr} - T_{\theta\theta}$ is independent of the Lagrange multiplier p (equation (12)), integrating equation (19a) gives

$$T_{rr} = \int_{r_2}^{r} \frac{T_{\theta\theta} - T_{rr}}{r} dr + T_{rr}|_{r=r_2}, \qquad (21)$$

where $T_{rr}|_{r=r_2}$ is the radial stress $r = r_2$. The internal pressure P is equal to $-T_{rr}$ at $r = r_1$. The Lagrange multiplier p is determined from equation (12). The resultant axial force acting in the z-direction on the plane $z = $ constant is

$$N_z = 2\pi \int_{r_1}^{r_2} rT_{zz} dr. \qquad (22)$$

However, we treat the cylinder as if it is closed at the ends so that the pressure P acting on the curved inside surface of the model left ventricle also acts on the plane ends to contribute an axial force resultant equal to $P\pi r_1^2$. Hence, the *net* axial force is

$$N_z = 2\pi \int_{r_1}^{r_2} rT_{zz} dr - P\pi r_1^2, \qquad (23)$$

or, substituting equations (12) and (21) into (22) (see Choung and Fung [23]),

$$N_z = 2\pi \int_{r_1}^{r_2} \left[T_{zz} - \frac{1}{2}(T_{rr} + T_{\theta\theta}) \right] r \, dr,$$

in which the integrand is independent of p. Similarly, the resultant torsional moment about the z-axis of the shear forces on this surface is

$$M_z = 2\pi \int_{r_1}^{r_2} r^2 T_{\theta z} dr. \qquad (24)$$

Numerical Techniques. The integrals in equations (21), (23) and (24) were evaluated by an adaptive routine (NAG Subroutine D01AJF [25]), using the Gauss 10-point and Kronrod 21-point rules. At each quadrature point, the circumferential and axial equations of equilibrium (equation (20)) could be solved simultaneously for the function $\partial\phi/\partial R$ and $\partial\omega/\partial R$ using a modification of the Powell hybrid method (NAG Subroutine C05NBF [25]). The accuracy of solutions was confirmed for special cases of materials possessing curvilinear aeolotropy against known analytical solutions [24].

Results

Kinematic Parameters. The prescribed kinematic parameters were determined from experimentally measured deformations in isolated potassium-arrested rat and dog heart preparations. First, the inflation, stretch and twist of the cylinder, defined by r_1, β and ϵ_2, respectively, were prescribed to match two-dimensional epicardial strains measured by McCulloch and coworkers [13] in the passive canine heart during static left ventricular loading. From the measured displacements of three epicardial markers 10–20 mm apart on the anterior free wall of six hearts, they computed mean major and minor principal stretches and associated principal directions at left ventricular cavity volumes of 115, 130, 145, 160, and 175 percent of the volume at zero transmural pressure. Here, these data are converted into the equivalent epicardial strains $E_{\theta\theta}$, E_{ZZ}, and $E_{\theta Z}$, and solved for the geometric and kinematic parameters βR_2, ϵ_2, and r_1/R_2 using equations (6b), (6c), and (6e) and the incompressibility constraint (equation (4)). Because these strains had been measured in the intact left ventricle and referred to the zero-pressure state, the residual strain parameters were $\alpha = 1$, $\epsilon_l = 1$ and $\gamma = 0$ for the purpose of finding βR_2, ϵ_2 and r_1/R_2, and we interpret r and R here as the radii of the ventricle in the loaded and zero-pressure (but not stress-free) states, respectively:

$$\beta R_2 = \frac{2E_{\theta Z}}{2E_{\theta\theta} + 1} \quad (\text{at } R = R_2),$$

$$\epsilon_2 = \sqrt{2E_{ZZ} + 1 - \frac{4E_{\theta Z}^2}{2E_{\theta\theta} + 1}} \quad (\text{at } R = R_2),$$

$$\frac{r_1}{R_2} = \sqrt{2E_{\theta\theta} + 1 - \frac{1 - \left(\frac{R_1}{R_2}\right)^2}{\epsilon_2}} \quad (\text{at } R = R_2).$$

Since the stress solutions are dependent only on the strains and material parameters, the numerical value of R_2 is entirely arbitrary. Assuming that volume changes in the cylinder and the left ventricle were comparable, the ratio R_1/R_2 of the model in the zero-pressure state was determined by considering the relative cavity volume ν/V, where ν is the deformed volume and V is the volume at zero left ventricular pressure:

$$\frac{\nu}{V} = \epsilon_2 \left(\frac{r_1}{R_1}\right)^2.$$

From the kinematic incompressibility constraint (equation (4)) and equation (6b) for circumferential strain at $R = R_2$, one may write a linear relationship between the epicardial circumferential strain and the relative cavity volume:

$$\frac{\nu}{V} = \left(\frac{R_2}{R_1}\right)^2 (2\epsilon_2 E_{\theta\theta} + \epsilon_2 - 1) + 1 \qquad (\text{at } R = R_2).$$

Using the measured mean epicardial circumferential strains and calculated extension ratios ϵ, the constant R_1/R_2 was com-

Table 1 Mean left ventricular volumes, pressures and epicardial strains measured in arrested canine hearts (McCulloch et al. [13]), and the corresponding parameters of a cylindrical model

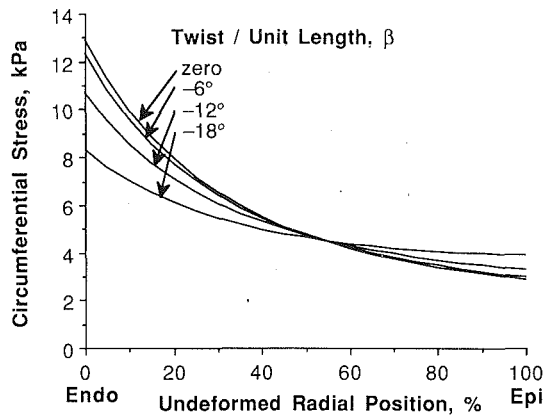| Relative volume %	Ventricular pressure kPa	Epicardial strains			Kinematic parameters[a]			
		$E_{\theta\theta} \times 10^2$	$E_{ZZ} \times 10^2$	$-E_{\theta Z} \times 10^2$	r_1/R_2	$-\beta R_2$ rad	ϵ	r_2/R_2
115	0.176	2.36	1.36	0.50	0.710	0.0095	1.014	1.023
130	0.424	4.76	3.05	0.82	0.749	0.0150	1.030	1.047
145	0.721	7.18	5.09	1.03	0.787	0.0179	1.050	1.069
160	1.102	8.36	8.80	1.71	0.812	0.0293	1.084	1.080
175	1.670	10.61	11.77	2.38	0.847	0.0393	1.111	1.101

[a] $R_1/R_2 = 0.671$

Fig. 3 Effect of torsion on transmural circumferential stress distribution in isotropic material model. Four curves are for various twists between 0 and −18 deg per unit nondimensionalized (by R_2) undeformed length. Left ventricular pressure 1.67 kPa; axial stretch 11.1 percent; no residual stress. The isotropic material parameters were chosen so that the model predicted the observed pressure volume curve.

Table 2 Material parameters of an isotropic model of the passive left ventricle with different stress-free states as determined by the "opening angle"

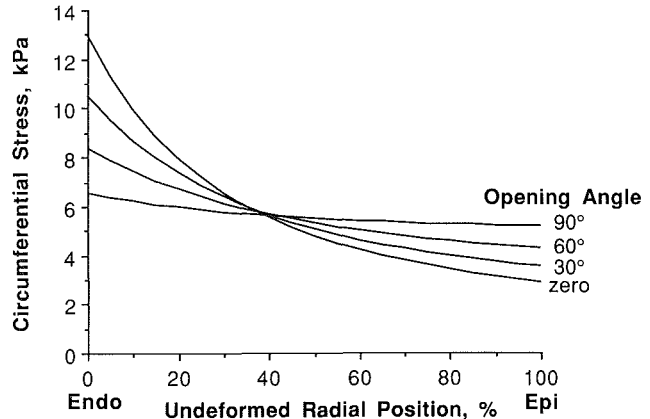| Opening angle deg	C kPa	b_1
0	0.765	4.24
30	0.740	4.41
60	0.711	4.57
90	0.677	4.72

Fig. 4 Effect of residual stress on transmural circumferential stress distribution for the isotropic material model at four opening angles between 0 and 90 deg. Relative left ventricular cavity volume 175 percent; axial stretch 11.1 percent; twist per unit length −2.25 deg. Stress-free radii and axial thickness were determined so that cavity pressure and axial force were zero in the unloaded state. For an isotropic material, a warping parameter of zero satisfied the requirement that the resultant torsional moment vanish.

puted that yielded the best fit to the reported volumes. Therefore, the kinematic parameters of the model have been derived from the pressure-strain behavior of the midanterior free wall region, while the reference dimensions have been chosen so that the model also describes the pressure-volume relation of the entire ventricle. The ratio $R_1/R_2 = 0.671$ gave the best fit to the relative volumes with a mean absolute error in the predicted volumes of 1.3 percent. This ratio agrees exceptionally well with the data from five diastolic canine hearts of Streeter and Hanna [26] who reported mean equatorial radii with a ratio of 0.672. The quantity r_2/R_2 was then determined at each volume from the experimentally measured circumferential strain $E_{\Theta\Theta}$. In Table 1, the kinematic parameters r_1/R_2, βR_2, γ and r_2/R_2 are listed at each of the five relative volumes, together with the corresponding left ventricular pressures that were reported [13].

Experimental measurements of the "opening angle" following radial resection of circumferential slices from the equatorial region of isolated, potassium-arrested rat hearts are the only quantitative data describing the left ventricular stress-free state [12]. For a 50 deg opening angle typical of the rat left ventricle, the kinematic parameter α is 1.161. However, since these observations were made from photographs in the circumferential plane, the axial stretch ratio ϵ_1 and warping parameter γ were not measured. For arteries, Choung and Fung [23] calculated the radii in the stress-free configuration from measurements of the perimeters at the inner and outer surfaces. They assumed that the axial thickness of the section remained constant, and they did not consider warping. We, however, computed the radii, axial stretch ratio and warping parameter corresponding to the absence of an inner pressure, a resultant torsional moment and a net axial force in the unloaded configuration. Therefore, the dimensions of the reference sector for a given opening angle were determined only after specifying the model material properties and obtaining an equilibrium solution.

Three-dimensional transmural strain measurements in the beating heart indicate that substantial transverse shears occur during systole [20]. Hence, one might expect that $E_{R\Theta}$ and E_{RZ} would be non-zero during passive filling. However, measurements of these strains have not yet been reported. Therefore, while these shear strains and the corresponding shear stresses are included in the general model, we assume for the purposes of solution that they are zero. Hence, from Appendix A (equations (A1d), (A1f)) the transverse shear stresses become zero and the equilibrium equations (19b,c) are satisfied trivially. Because the measured strain data used to validate the model were from isolated hearts with the right ventricle vented to

atmosphere [13], the stress boundary conditions were defined by the measured left ventricular pressures applied at the endocardium alone.

Isotropic Material Models. First, the special case of the constitutive law in which the material properties were isotropic and therefore independent of fiber orientation was considered. Then, there were only two non-zero material parameters in equation (13), C and b_1, and the exponent became

$$Q = 2b_1(\overline{E}_{RR} + \overline{E}_{FF} + \overline{E}_{CC}) = 2b_1(E_{RR} + E_{\Theta\Theta} + E_{ZZ}).$$

These parameters were optimized using an unconstrained nonlinear least squares algorithm (NAG Subroutine E04FDF [25]) so that the model fitted the experimentally observed pressure-volume relation for the case of inflation, stretch and twist with no residual stress. Estimates of the variances of the estimated coefficients were determined from the diagonal terms of the covariance matrix (NAG Subroutine E04YCF [25]). Using the kinematic parameters from Table 1 with $\alpha = 1$, we found that the material parameters $C = 0.765$ kPa and $b_1 = 4.24$ produced predicted cavity pressures that were closest to the experimental results (SD = 0.030 kPa) at the five ventricular volumes reported.

The effect of increasing twist on the transmural distribution of circumferential stress is demonstrated in Fig. 3 for the isotropic materials model. Here, the torsion parameter β was varied between zero and −18 deg of twist per unit nondimensionalized (by R_2) undeformed length, while the pressure load and stretch of the cylinder were maintained at 1.672 kPa and 11.1 percent, respectively. In each case, the deformed radii were corrected so that the pressure was constant regardless of the prescribed torsion. Thus, the relative volume changes decreased somewhat from 175 percent as the twist was increased. The model predictions indicate that the high transmural circumferential stress gradients in the isotropic model are reduced by torsion (by approximately 40 percent for a twist of −18
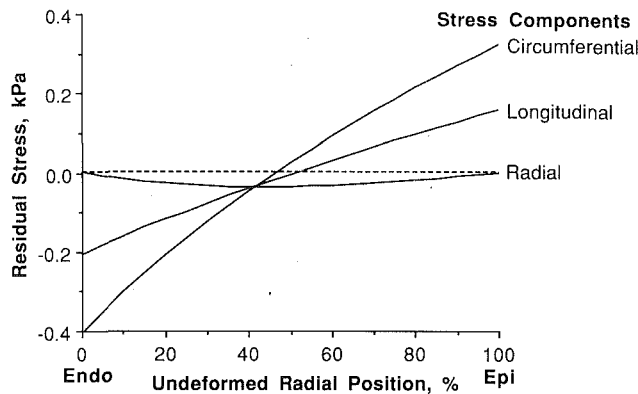
Fig. 5 Transmural profiles of residual stress in isotropic model of un-loaded left ventricle for a 50 deg opening angle
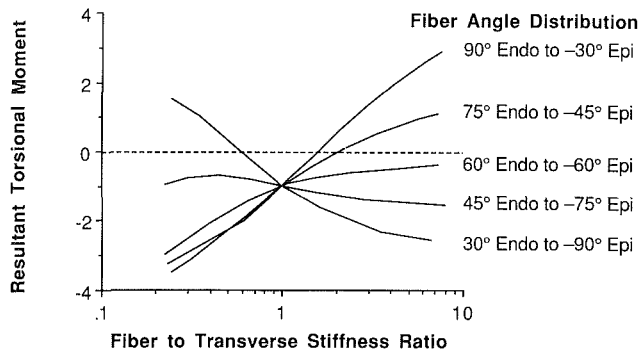

Fig. 6 Effect of fiber-to-transverse stiffness ratio (ratio of material stiffness in the fiber direction to stiffness in the transverse plane that would be measured in a plane equibiaxial extension of 20 percent) and transmural fiber angle distribution on the applied torsional moment required to produce the observed epicardial shear. Relative left ventricular cavity volume 175 percent; opening angle 50 deg (see Table 1 for kinematic parameters). The torsional moment is normalized by the absolute value of that for the isotropic model. A zero fiber angle corresponds to the circumferential axis. A stiffness ratio of one corresponds to isotropy. A nonzero warping parameter was required so that the unloaded config-uration of the anisotropic models could be maintained without applying a resultant torsional moment.

deg per unit length). Furthermore, equal increments of twist resulted in greater and greater decreases in the endocardial stress maxima.

The influence of residual stress on the transmural distribution of circumferential stress is shown in Fig. 4 for the isotropic material model at 175 percent volume inflation, axial stretch of 11.1 percent and twist of -2.25 deg per unit length. Here, the residual stress was increased by increasing the initial opening angle from 0 to 90 deg. The isotropic material parameters were adjusted so that the model comparisons were made for matching pressure-volume curves at each opening angle, and are listed in Table 2. Compressive residual stress at the endocardium increased with opening angle and hence decreased the tensile endocardial circumferential stress present during filling (by approximately 50 percent for an opening angle of 90 deg). The transmural profiles of residual stress in an isotropic model of the unloaded LV are shown in Fig. 5 for a 50 deg opening angle ($\alpha = 1.161, C = 0.721$ kPa, $b_1 = 4.52$). In this case, circumferential and longitudinal stresses were small near midwall, increasingly compressive toward the en-docardium and increasingly tensile approaching the epicar-dium.

Aeolotropic Material Models. Although the isotropic models with various twists and opening angles could all be matched to the observed pressure-volume and strain data, none of them would twist and stretch the prescribed amount under pressure loading alone. A net axial force and torsional moment
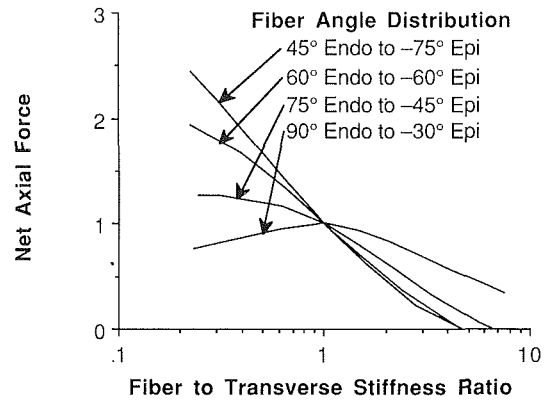

Fig. 7 Effect of anisotropy (see Fig. 6 legend) and transmural fiber angle distribution on the applied net axial force (difference between the resultant force due to axial stress in the wall and that resulting from the cavity pressure acting on the closed ends of the cylinder) required to produce the experimentally observed stretch. Relative left ventricular cavity volume 175 percent; opening angle 50 deg (see Table 1 for kine-matic parameters). The net axial force is normalized by the isotropic model value.

were required to maintain the deformation (see equations (23) and (24)). Therefore, the effect of anisotropy and transmural fiber angle distribution on the magnitudes of the torsional moment and net axial force accompanying these prescribed deformations was examined. The simplest type of material symmetry that will allow a difference in fiber and cross-fiber properties as has been observed experimentally [10] is that of transverse isotropy [27]. On structural grounds [28], the pre-ferred axis of material symmetry was chosen to be the local muscle fiber direction. The elastic stiffness along the fiber axis or in the transverse plane was increased independently by in-creasing either b_2 or b_3, respectively, from zero with C and b_1 optimized to predict the pressure-volume relation. The ani-sotropy was characterized by the ratio of material stiffness in the fiber direction $dT_{ff}/d\lambda$ to stiffness in directions transverse to the fibers $dT_{cc}/d\lambda$ subject to a plane equibiaxial extension λ (see Appendix 2).

The effect of varying the fiber-to-transverse stiffness ratio over a wide range on the magnitude of the torsional moment (equation (24)) required to produce the observed epicardial shear strain is shown in Fig. 6 for five different fiber angle distributions and an opening angle of 50 deg. Here, the tor-sional moment is normalized by the absolute value for the isotropic model. These results indicate that the torsional mo-ment is reduced to zero by increasing the fiber stiffness for fiber angle distributions in which the circumferential fibers are closer to the epicardium than the endocardium. Increasing the transverse stiffness reduces the torsional moment to zero for fiber angle distributions in which the circumferential fibers are shifted sufficiently toward the endocardium. For intermediate fiber angle distributions where the circumferential fibers are in the midwall, the resultant moment remains negative over a wide range of stiffness ratios.

The influence of varying the fiber-to-transverse stiffness ra-tio over a wide range on the magnitude of the net axial force required to produce the observed epicardial longitudinal strain is shown in Fig. 7 for four different fiber angle distributions. Here, the net axial force (equation (23)) tends to decrease monotonically with increasing stiffness ratios for most fiber angle distributions. In general, stiffness ratios corresponding to zero net axial force were greater than those yielding zero moment, but this difference was smallest for a fiber angle distribution of 75 deg (endocardium) to -45 deg (epicardium). For this fiber angle distribution the fiber-to-transverse stiffness ratio at which the applied torsional moment vanished was 2.1. The net axial force was zero when the ratio was 6.7. It is noteworthy that the mean midanterior epicardial fiber angle
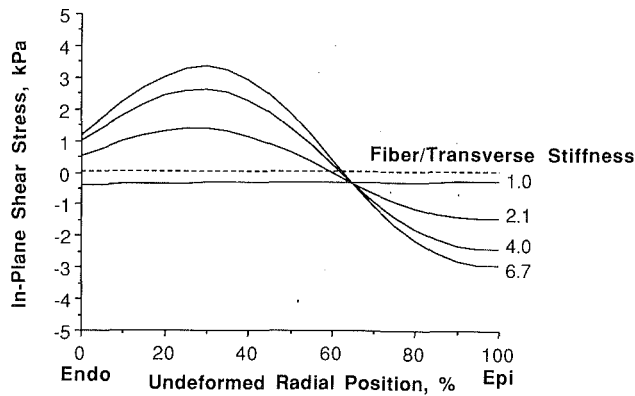
Fig. 8 Effect of the transition from isotropy to anisotropy on the transmural distribution of in-plane shear stress for the prescribed displacements corresponding to experimental measurements of epicardial strain by McCulloch et al [13] (see Table 1). Relative left ventricular cavity volume 175 percent; opening angle 50 deg; linear fiber angle variation from 75 deg (endocardium) to −45 deg (epicardium). The applied torsional moment vanished at a fiber-to-transverse stiffness ratio of 2.1. Similarly, the net axial force is zero for a stiffness ratio of 6.7.
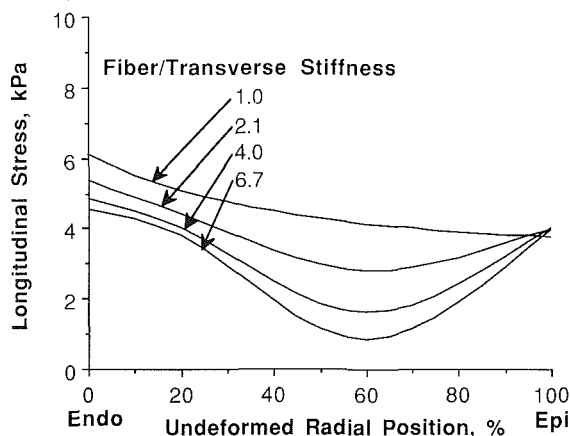

Fig. 9 Effect of the transition from isotropy to anisotropy on the transmural distribution of longitudinal stress. See legend of Fig. 8.

reported by McCulloch et al. [13] was −42±7 deg. Waldman and coworkers [29] found similar epicardial fiber orientations. In that study the transmural distributions of fiber direction were typically quite linear through 70 to 80 percent of the wall thickness plateauing in the longitudinal direction near the endocardium. Linear regressions on the fiber angle data as a function of percent depth in the anterior free wall of seven canine left ventricles yielded average slopes of 1.56±0.14 deg/percent depth and an average epicardial intercept of −49±15 deg. Finally, the more extensive measurements of Nielsen and colleagues [30] show fiber angles of −46 deg on the epicardium and 88 deg on the endocardium at exactly the same location where the experimental measurements had been made. It should be noted that in the canine anterior wall the fiber angle distribution may be quite nonsymmetric with respect to midwall [29,30].

The effects of the transition from isotropy to anisotropy on transmural stress profiles at a relative volume of 175 percent (Table 1) are shown in Figs. 8 to 10. Here, the fiber-to-transverse stiffness ratio has been increased from 1.0 (isotropy) to 6.7. Figure 8 shows the transmural profile of shear stress $T_{\theta z}$, which determines the torsional moment (equation (24)). Notice how the shear stress changes sign near the point where the fibers are circumferential. The axial force (equation (22)) is determined by the transmural distribution of longitudinal stress plotted in Fig. 9. Although the longitudinal stress falls off monotonically as a function of radius in the isotropic case, increasing stiffness ratios are accompanied by decreasing stress
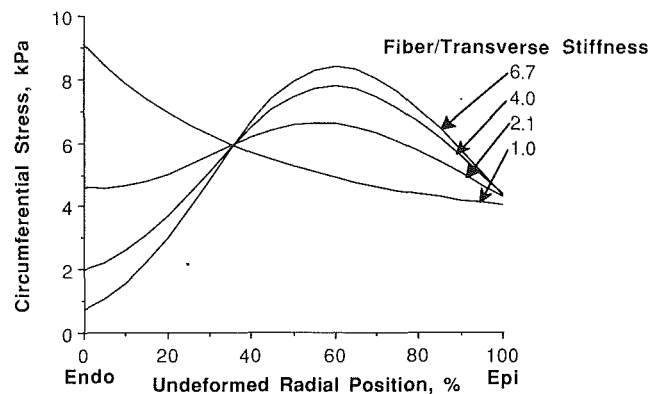

Fig. 10 Effect of the transition from isotropy to anisotropy on the transmural distribution of circumferential stress. See legend of Fig. 8.

minima occurring near the circumferential fibers. Figure 10 shows how increasing the fiber-to-transverse stiffness ratio reduces the endocardial peak in circumferential stress and increases the subepicardial values. Similar to the longitudinal stress, circumferential stress falls off monotonically with radius in the isotropic case, but with increasing stiffness ratio these profiles become non-monotonic with stress peaks occurring near the circumferential fibers. The large reduction in endocardial circumferential stress with an increase in the stiffness ratio is due to the more longitudinal orientation of muscle fibers there.

Parameter Estimation. The results in Figs. 6 and 7 show that the fiber stiffness must be greater than the transverse stiffness to minimize both the applied force and moment required to cause the measured epicardial strains. Therefore, with $b_3 = 0$ optimal estimates for C, b_1, b_2, and b_4 (b_4 changes the modulus of shear in planes parallel to the fiber axis of the material) were sought. Simultaneously, we minimized the sums of the squares of the resultant torsional moments, the net axial forces, and the differences between experimental and model-predicted cavity pressures for the measured deformations at all five left ventricular volumes shown in Table 1. It is preferable for the objective functions (squared pressure differences, moments and forces) to be of the order of unity in the region of the optimal solution [31]. First, the optimization was performed without scaling of objective functions. Then, the optimization was repeated with each function scaled by the mean values from the previous solution. When the scaling factors had converged, the optimal estimates for the material parameters were independent of the initial estimate, indicating that the global minimum has been obtained. The variances of the optimal coefficients were also determined.

Table 3 shows the effect of varying the fiber angle distribution on the optimal parameters assuming a 50 deg opening angle. Corresponding values from the isotropic material model are included for comparison. The predicted fiber-to-transverse stiffness ratio varied from 2.82 to 6.62 for the three fiber angle distributions. The minimized pressure differences and resultants, and the confidence intervals for the material parameter estimates are shown also in Table 3. Comparing these for the three fiber angle distributions shows that the parameter estimates were best when the fiber angle varied from 75 deg at the endocardium to −45 deg at the epicardium, which is consistent with the results shown in Figs. 6 and 7. The estimates of C, b_1 and b_2 were not over-sensitive to fiber angle distribution in the range studied, and in all cases the standard deviation about the predicted parameter was less than 7 percent. However, the shear parameter b_4 was poorly determined and highly sensitive to fiber angle. In one instance, it was negative, which is physically unacceptable.

Table 3 Optimized material parameters, and mean pressure differences and resultants of an anisotropic model of the passive left ventricle for three linear transmural fiber angle distributions

Fibre angle[a] deg	$C \pm \sqrt{\mathrm{var}\ C}$ [b] kPa	$b_1 \pm \sqrt{\mathrm{var}\ b_1}$	$b_2 \pm \sqrt{\mathrm{var}\ b_2}$	$b_4 \pm \sqrt{\mathrm{var}\ b_4}$	ΔP kPa	$\dfrac{M_z}{R_2^3}$ kPa	$\dfrac{N_z}{R_2^2}$ kPa
60, −60	0.875 ± 0.090	1.243 ± 0.174	17.50 ± 1.092	−4.14[c] ± 1.517	0.020 ± 0.027	0.031 ± 0.039	0.038 ± 0.048
75, −45	0.644 ± 0.085	2.547 ± 0.248	15.09 ± 1.284	10.48 ± 1.898	0.028 ± 0.037	0.018 ± 0.023	0.183 ± 0.226
90, −30	0.562 ± 0.087	3.185 ± 0.323	15.38 ± 2.314	23.85 ± 5.059	0.030 ± 0.042	0.031 ± 0.050	0.346 ± 0.444
isotropic[d]	0.721 ± 0.084	4.521 ± 0.298	00.00 ± 0.000	00.00 ± 0.000	0.023 ± 0.032	0.203 ± 0.294	1.294 ± 1.864

[a]Endocardial, epicardial fiber angles, respectively, for a linear fiber angle distribution.
[b]Note: If x′ is the true solution, then the $100(1 - \beta)$ confidence interval on the solution x is

$$x_i - \sqrt{\mathrm{var}\ x_i} \cdot t_{(\beta/2,n)} < x_i < x_i + \sqrt{\mathrm{var}\ x_i} \cdot t_{(\beta/2,n)}, \quad \{x_1, x_2, x_3, x_4\} = \{C, b_1, b_2, b_4\}$$

where $t_{(\beta/2,n)}$ is the $100\beta/2$ percentage point of the t-distribution with n degrees of freedom (3 for isotropy; 11 for anisotropy).
[c]Note that a negative predicted parameter is not physically acceptable.
[d]Note that only C and b_1 were optimized by minimizing pressure differences.

Table 4 Optimized material parameters of an anisotropic model of the passive left ventricle with different opening angles

Opening angle deg	$C \pm \sqrt{\mathrm{var}\ C}$ [b] kPa	$b_1 \pm \sqrt{\mathrm{var}\ b_1}$	$b_2 \pm \sqrt{\mathrm{var}\ b_2}$	$b_4 \pm \sqrt{\mathrm{var}\ b_4}$	ΔP kPa	$\dfrac{M_z}{R_2^3}$ kPa	$\dfrac{N_z}{R_2^2}$ kPa
0	0.641 ± 0.082	2.929 ± 0.268	10.82 ± 0.746	14.08 ± 2.224	0.029 ± 0.038	0.024 ± 0.028	0.198 ± 0.246
25	0.641 ± 0.084	2.740 ± 0.261	13.10 ± 1.012	12.69 ± 2.178	0.029 ± 0.038	0.021 ± 0.026	0.195 ± 0.242
50	0.644 ± 0.085	2.547 ± 0.248	15.09 ± 1.284	10.48 ± 1.898	0.028 ± 0.037	0.018 ± 0.023	0.183 ± 0.226

The effect of varying the opening angle on the predicted parameters using a fiber angle distribution of 75 deg (endocardium) to −45 deg (epicardium) is shown in Table 4. The optimal estimates for the parameters of C and b_2 decreased while those for b_1 and b_4 increased as the opening angle was reduced from 50 deg to zero. The fiber-to-transverse stiffness ratio only varied from 2.41 to 3.29 for the model materials with opening angles of zero and 50 deg, respectively. Again b_4 was the parameter most sensitive to changes in the model assumptions.

The minimized torsional moment and net axial force for a fiber angle distribution of 75 deg (endocardium) to −45 deg (epicardium) were 8.4 and 13.9 percent, respectively, of those in the isotropic model, but they were not exactly zero (Table 3). Therefore, using these optimized anisotropic material parameters and the exact stress boundary conditions, the equations of equilibrium (equations (21), (23) and (24)) were solved with the displacements (inflation, stretch and twist) as the unknowns. In Fig. 11, the predicted epicardial major and minor principal extensions and principal directions of the major stretch are compared with the experimental measurements [13] in the isolated potassium-arrested dog heart for cavity pressures ranging from zero to 2.0 kPa. All the principal extensions and principal directions were within or extremely close to one standard error (= SD/√n) of the experimental measurements at all loads. The left ventricular volumes predicted from prescribed pressure loading were all within 1.3 percent (0.5 ml) of the measured values.

With the optimal material parameters given in Table 4 for a 50 deg opening angle, the transmural profiles of fiber strain were computed by allowing the model to equilibrate with the full range of cavity pressures alone as described above. In Fig. 12, the predicted fiber strain profiles are compared with transmural sarcomere length distributions computed from experimental measurements by Grimm and coworkers [32] in the cadmium-arrested rat heart. Both the model predictions and the experimental measurements are non-monotonic with fiber strains peaking in the outer half of the wall at all ventricular pressures. This was observed also in the one adult dog studied by Grimm and co-workers. Note their close agreement at the highest load.

The profiles of stress referred to fiber coordinates as predicted with the same model for a cavity pressure of 1.67 kPa are shown in Fig. 13. Again the fiber stresses are non-monotonic with a slight peak in the outer half of the wall. Cross-
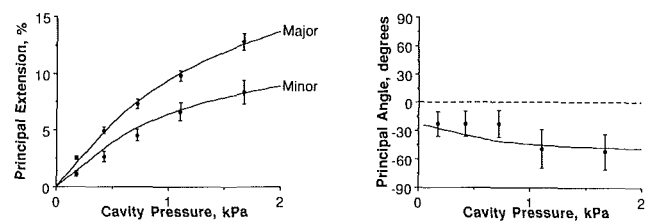

Fig. 11 Comparison of predicted epicardial major and minor principal extensions (left) and principal directions of the major stretch (right) with the experimental measurements by McCulloch et al. [13] in the dog heart for a range of ventricular pressures. Opening angle 50 deg, linear fiber angle variation from 75 deg (endocardium) to −45 deg (epicardium). Model principal extensions and principal angle (curves) were determined by matching the prescribed cavity pressures and requiring the resultant torsional moments and net axial forces to vanish in the loaded state. The error bars on the experimental measurements (solid circles) indicate one standard error of the mean.
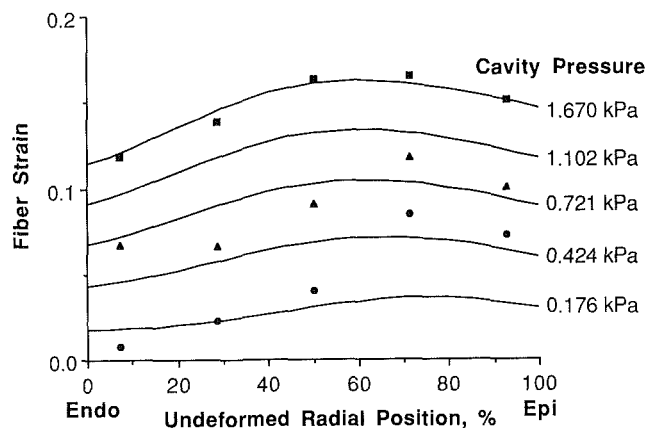

Fig. 12 Comparison of transmural fiber strain distributions with those calculated from experimental measurements of sarcomere lengths across the wall of the rat heart by Grimm et al. [32] for a range of ventricular pressures. Opening angle 50 deg, linear fiber angle variation from 75 deg (endocardium) to −45 deg (epicardium). Model predictions (curves) are shown for five left ventricular cavity pressures. Model displacements were determined by equilibrating model with prescribed cavity pressure only. Sarcomere (Lagrangian) strains for low (circles), medium (triangles) and high (squares) cavity pressures are referred to the average sarcomere length at zero left ventricular pressure.
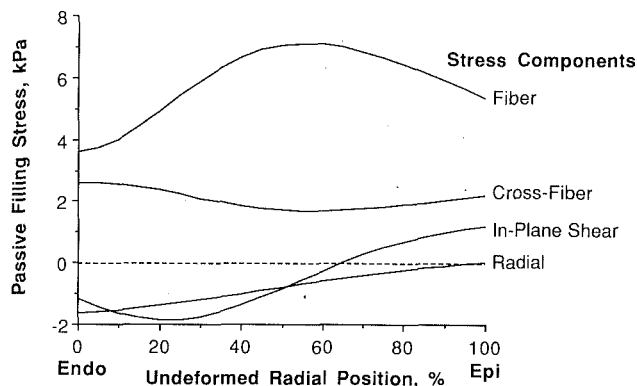
Fig. 13 Profiles of stress referred to fiber coordinates at a left ventricular cavity pressure of 1.670 kPa. Opening angle 50 deg, linear fiber angle variation from 75 deg (endocardium) to − 45 deg (epicardium). Displacements were determined by equilibrating model with prescribed cavity pressure only. This model material has a fiber-to-transverse stiffness ratio of 3.29 as defined in the text.

fiber stress is uniform and the in-plane shear stress referred to fiber coordinates changes sign near mid-wall as was seen for the anisotropic models in Fig. 8. If residual stress were not taken into account, the fiber stress and strain distributions predicted with the model were similar to those in Figs. 12 and 13 except that the peaks were shifted toward midwall.

Discussion

Myocardial strain distributions in the intact left ventricle have been determined by measuring the displacements of closely spaced markers [20, 29, 33] or length transducers [34, 35] implanted in the ventricular wall, but the direct measurement of local forces or stresses in the intact heart wall has not been reliable [9, 36]. An alternative approach to determine ventricular wall stress is mathematical modeling based on the conservation laws of continuum mechanics [37]. However, the task of realistically modeling the complex three-dimensional geometry and fiber architecture, the large deformations and the nonlinear, anisotropic, time-dependent material properties of even the left ventricle alone is extremely difficult. Therefore, most continuum mechanics models of the heart have been restricted to the passive left ventricle and have relied either on simplified geometric representations, such as cylinders [2, 14, 15, 17] or spheres [38–40], or on linear approximations to the governing equations [41, 42]. If all that is required of a model is that it reproduces global pressure-volume relationships, then mathematical sophistication is not required [37]. Even linear models based on cylindrical or spherical approximations are able to reproduce the diastolic filling curve to within 20 percent [43]. However, the importance of accounting for the large deformations of the passive left ventricle when predicting stress distributions has been demonstrated with finite element models [43] and is supported by experimental measurements of myocardial fiber stretches that may exceed 20 percent at physiological filling pressures. Moreover, no theoretical model has been validated independently by comparing predicted strain distributions with regional deformations measured in an appropriate intact experimental preparation. Other factors that have not been investigated fully in the stress analysis of the passive left ventricle include the influence of fiber architecture and the effects of residual stresses in the unloaded ventricle [12].

Both uniaxial and biaxial material testing of myocardium have been performed *in vitro* and used to propose stress-strain relations for passive myocardium [10, 44–48], but the applicability of these studies to the intact heart is not known. Moreover, passive material properties determined from pressure-volume data [38–40] are insensitive to regional variations

in ventricular mechanics. Therefore, a potential advantage of the current model is that its predictions such as material properties, stresses and strains are made while a close correlation with available global and regional measurements is maintained. The model matches both the observed pressure-volume relation and the measured two-dimensional finite strains occurring on the epicardium under physiologic loading. In addition, the left ventricle is modeled as a three-dimensional anisotropic material while avoiding the assumptions associated with nested membranes or thick-shell theories.

The helical fibrous structure of the ventricular myocardium has long been recognized by anatomists, but it is only in relatively recent times that improved histological techniques have helped to replace the traditional concept of discrete muscle bundles with the current descriptions of a smoothly continuous transmural variation in myofiber orientation [49]. The significance of this fiber arrangement to the mechanics of the actively contracting heart has been discussed at length and studied using axisymmetric geometric models with embedded fibers [16, 50]. In contrast, the potential influence of the fiber architecture on the mechanics of the diastolic heart has received less attention, and most models of the passive left ventricle have assumed isotropic material properties, which are independent of fiber direction. However, there is now considerable evidence that the passive myocardium is anisotropic with respect to its local fiber axis. Ultrastructural studies of myocardium indicate an extensive collagen skeleton that appears to tether adjoining fibers in the transverse plane [51, 52]. These observations have motivated the use of a transversely isotropic constitutive equation based either on a microstructural [48] or phenomenological [27] model. The effect of interrupting these transverse links when performing isolated muscle tests is not known.

Indirect evidence of anisotropy in the passive myocardium also comes from experimental studies of ventricular deformations. In the isolated potassium-arrested dog heart, McCulloch and coworkers [13] found that the principal direction of major epicardial stretch during passive left ventricular filling consistently coincided with the local fiber direction and not with either of the principal geometric axes. Moreover, the twist of the ventricle about the longitudinal axis was consistent with the preferential extension of the epicardial fiber helix during passive filling. Based on these findings, the authors suggested that, on the epicardium, the passive cardiac muscle is anisotropic, possibly with greatest compliance in the fiber direction. Alternatively, they speculated, these observations might be explained if the passive myocardium is stiffer in the fiber direction at all depths with endocardial fibers dominating the epicardial shear associated with diastolic torsion. The results of the current models support the latter explanation. Because the end-diastolic fiber strain determines systolic function, accounting for this anisotropy will be essential for an accurate assessment of the mechanics of the beating heart.

Another important difficulty that has not been addressed in previous models of ventricular mechanics is the stress-free state of the passive myocardium. To date, it has been assumed that when the transmural pressure gradient is zero, the intact ventricular wall is stress-free. However, recently it has been shown that the unloaded left ventricle is not stress-free. Omens and Fung [12] have demonstrated that when a cross-sectional ring of the freshly-excised potassium-arrested rat heart is cut radially, it springs open to form an arc. The 'residual' strains that they measured were generally consistent with a bending deformation required to restore the ring to its intact shape. The corresponding residual stresses in the unloaded left ventricle have not been included in previous models. However, new measurements should be performed in the canine ventricle to corroborate residual strains observed in the rat and rabbit, and to quantify any differences in the larger ventricle. If possible, it would be useful to measure passive loading strains and residual strains in the same hearts. Although these data are

not yet available, our analysis shows that, while the effect of the assumed opening angle on predicted circumferential stresses was significant, the basic conclusions of the parameter optimizations were not overly sensitive to this variable.

In our approach to this parameter estimation problem, optimal estimates for parameters of an exponential strain-energy function were obtained by minimizing the sum of the squared differences between experimental and predicted cavity pressures, torsional moments and net axial forces for prescribed displacements that gave rise exactly to experimentally measured epicardial strains. To verify that a global minimum has been obtained, the optimization was repeated for a wide range of initial parameter values. Also, variances for each parameter were determined. An alternative approach would be to prescribe strains. In general, however, for particular values of surface tractions and a given strain-energy function, a solution to the equilibrium equations may not exist or be unique [24]. Nevertheless, with our optimal material parameters, the equilibrium equations were solved for the unknown displacements subject to the known ventricular pressures and resultants, and solutions were obtained which agreed with experimental measurements of epicardial strain and transmural sarcomere lengths to well within experimental accuracy.

Humphrey and Yin [47] have fitted transversely isotropic exponential strain-energy functions directly to data from equibiaxial tests of isolated slices of passive canine myocardium [10]. Stresses predicted using their mean parameters were compared with those predicted using our optimal parameters in the case of equibiaxial stretch. For equibiaxial extension ratios from 1.01 to 1.09, the material model of Humphrey and Yin [47] predicts a ratio of fiber stress to cross-fiber stress that remains relatively constant varying from 3.0 to 2.8. Using our optimal parameters, the ratios are slightly lower varying from 2.1 to 2.4. However, the magnitudes of fiber stresses predicted by Humphrey and Yin's law are 3.5 to 4.3 times those found currently. This comparison suggests that whereas the predicted anisotropy of the myocardium is very similar in each study, the constitutive law based on the isolated tissue experiments [10] would significantly underestimate global ventricular compliance. It is possible that this discrepancy is due to contracture of the isolated muscle specimens. Moreover, the damaging effects of resecting and tethering the specimens are unknown.

Our constitutive law contained five parameters of which only four were optimized since either b_2 or b_3 was zero. Alternatively, one could set $b_1 = 0$. The resulting transversely isotropic strain-energy function has the advantage that it can be inverted numerically to uniquely express strains as a function of stress components [54] and the hydrostatic pressure is zero in the stress-free state. Therefore, the optimization was repeated with $b_1 = 0$ and C, b_2, b_3, and b_4 unknown; and, again, material parameters were found that were globally optimal. The corresponding fiber-to-transverse stiffness ratio predicted with these parameters was 3.29, identical to that found when the isotropic term was a linear function of strain components. These results suggest that the alternative quadratic form may be equally suitable.

The myocardium like all soft tissues is mostly water. Therefore, without perfusion it has been found to be close to incompressible [22]. By enforcing the kinematic incompressibility constraint in our model, the contribution of fluid to the model material properties is introduced via the hydrostatic pressure variable p. In the living tissue, fluid shifts due to coronary perfusion or edema may occur. The experimental strains used currently were measured in unperfused isolated hearts. It has been shown that increased coronary artery pressure increases the slope of the diastolic pressure-volume relation. How the effect of fluid in myocardium should be modeled remains unclear but single and multiple compartment models have been proposed by Bogen [55, 56].

The predictions of the cylindrical model are based only on two-dimensional epicardial strain measurements. Three-dimensional transmural strain measurements in the beating heart indicate that substantial transverse shears often accompany normal strains during systole, and that systolic strains tend to increase with depth beneath the epicardium [20, 29]. However, correlation of the model with three-dimensional strain data will require new measurements (currently being undertaken in our laboratory) in the diastolic or arrested heart under appropriate loading conditions. Moreover, in a cylindrical model, external surface tractions are required to produce such transverse shears. But these tractions are not realistic because the transverse shears may arise from the doubly-curved geometry of the left ventricle. Other three-dimensional effects that cannot be incorporated in the current model include circumferential and longitudinal variations in stress and strain. These effects result from factors such as ventricular interactions, the boundary constraint due to the tethering of myocardium to the valve rings, the base-to-apex variation of curvature, and the nonaxisymmetric geometry. Consideration of these additional complexities requires a detailed finite element analysis of ventricular mechanics currently underway in our laboratory.

Several studies that have accounted for transmural fiber angle variations have assumed a cubic variation apparently on the strength of Fig. 4 in Streeter et al. [49] where fiber angles tended to change most rapidly at the endo- and epicardium and were more uniform near the midwall. However, the mean distributions reported in the same article (Fig. 5) show much less nonlinearity. Nielsen and coworkers [30] have recently made much more extensive measurements in isolated hearts fixed under the same conditions as the hearts from McCulloch and colleagues [13], whose deformation data were used in our model. Their findings show a more complex fiber angle distribution that even peaks and reverses near the subendocardium. Significant regional variations were also found. For these reasons any single higher order polynomial description of fiber angle is difficult to justify statistically. Moreover, a careful examination of numerous fiber angle measurements [29,30,49] indicates that the distributions are often nonsymmetric with respect to midwall. As indicated by the current results, these nonsymmetric distributions seem to have certain advantages, e.g., the resultant torsional moment is nonzero over a wide range of fiber-to-transverse stiffness ratios for a symmetric (albeit linear) distribution (see Fig. 6: 60 to -60 deg curve). On the other hand, for many of the nonsymmetric distributions, the moment is zero at reasonable values of the stiffness ratio (Fig. 6: 75 to -45 deg curve and 90 to -30 deg curve). It is important to recognize that the computed stress profiles can be quite sensitive to the local fiber orientation. In addition, the presence of any transmural or regional variation in material properties also could significantly change the computed stresses. Thus, the assumption of material homogeneity common to this study and virtually all others means that the material parameters must be considered "effective moduli." In the future it would be relatively easy in the simplified geometries to demonstrate the influence of transmural fiber distributions that are both nonlinear and nonsymmetric and transmural variations in material properties, but studying the influence of regional variations in fiber architecture and material heterogeneity in a more realistic three-dimensional geometry is a much more difficult task.

Very recently, Humphrey and Yin [17] proposed a cylindrical model of the equatorial region of a passive left ventricle not in an effort to determine material properties, but to estimate the transmural distributions of stress and strain in this region. Analogous to our approach, they prescribed displacements determined from experimental strain data. Their analysis serves as an important contribution to cardiac mechanics because they accounted for the local transverse stiffness of the myocardium and for the potential influence of transverse shearing stresses and strains. However, they employed only one time

series of strains referred to end-diastole from the study of Waldman and coworkers [20] at one transmural location in a single beating open-chested canine heart. These measurements are less suitable for our purposes than those of McCulloch and coworkers [13] for a number of reasons: the boundary and loading conditions are less accurately defined in the in-vivo preparation, e.g., the right ventricle was vented to atmosphere in the isolated heart; the ventricular volumes were not measured in the beating heart preparation; the extent to which the diastolic filling left ventricle can be considered passive is uncertain; the dynamic effects of diastolic filling were minimized in the isolated preparation by static loading; the isolated heart was unperfused, whereas coronary blood flow varies continuously throughout the cardiac cycle in vivo; and the measurement error in strain was considerably lower in the isolated heart. Moreover, in the study of Humphrey and Yin, residual stress was not taken into account and the undeformed radii were determined from a different experimental study.

In contrast to our model, their prescribed model displacements produced in-plane shear strains that were positive throughout the wall. It is possible that their reanalysis of the systolic strain measurements of Waldman and coworkers [20] was incorrect. When we recomputed strains during diastole using the original three-dimensional coordinates of the myocardial markers both the in-plane torsional shear and transverse axial shear were negative, not positive as they found. The negative torsional shear is in agreement with the measurements [13] with which our analysis was correlated. These negative shears have an influence on the stress profiles that is profoundly different from positive shears, i.e., they result in stress profiles that tend to be much more uniform without the endocardial stress concentrations often found in pressure vessel studies. In fact, in the vast majority of pressure vessel analyses including fluid-fiber cylindrical models [2, 14, 15, 17], circumferential or fiber stress maxima occur at or near the inner wall. While the presence of torsion [16, 53] has been shown to reduce large endocardial stress gradients in the systolic left ventricle and residual stress reduces these gradients at the inner wall of arteries [23], the current results indicate that torsion, residual stress and material anisotropy associated with the fiber architecture all can act to reduce endocardial stress gradients in the passive left ventricle. As a result, stress and strain components may vary non-monotonically with radius. In particular, subendocardial concentrations of circumferential and fiber stresses may be unrealistic; these stress profiles may be more uniform or have maxima in the outer half of the ventricular wall.

Although the assumption of a cylindrical model is an oversimplification of the complex three-dimensional geometry of the left ventricle, it may be a reasonable approximation of the equatorial region. If so, it allows us to account for many of the other complex features of ventricular mechanics without the use of sophisticated computational techniques such as finite element analysis. Moreover, until the utility of simpler models is fully exploited and more experimental data are obtained, a three-dimensional finite element analysis would be premature. Among the features incorporated in the current model of the passive left ventricle are its nonlinear, anisotropic material properties, fiber architecture, and large deformations including the influence of torsion and residual stress as the ventricle inflates and lengthens. Thus, the current analysis can be used as a check for future finite element approximations. Moreover, the optimized parameters in the constitutive equation provide an initial estimate when a similar approach is applied with a more realistic geometry using the finite element method.

Acknowledgments

References

1 Sarnoff, S. J., Braunwald, E., Welch, G. H. Jr., Case, R. B., Stainsby, W. N., and Macruz, R., "Hemodynamic Determinants of Oxygen Consumption of the Heart with Special Reference to the Tension-Time Index," *Am J Physiol,* Vol. 192, 1958, pp. 148–156.

2 Jan, K.-M., "Distribution of Myocardial Stress and Its Influence on Coronary Blood Flow," *J Biomech,* Vol. 18, 1985, pp. 815–820.

3 Lew, W. Y. W., "Influence of Ischemic Zone Size on Nonischemic Area Function in the Canine Left Ventricle," *Am J Physiol,* Vol. 252, 1987, pp. H990–H997.

4 Theroux, P., Ross, J. Jr., Franklin, D., Covell, J. W., Bloor, C. M., and Sasayama, S., "Regional Myocardial Function and Dimensions Early and Late After Myocardial Infarction in the Unanesthetized Dog," *Circ Res,* Vol. 40, 1977, pp. 158–165.

5 Bogen, D. K., Rabinowitz, S. A., Needleman, A., McMahon, T. A., and Abelmann, W. H., "An Analysis of the Mechanical Disadvantage of Myocardial Infarction in the Canine Left Ventricle," *Circ Res,* Vol. 47, 1980, pp. 728–741.

6 Bogen, D. K., Needleman, A., and McMahon, T. A., "An Analysis of Myocardial Infarction: The Effect of Regional Changes in Contractility," *Circ Res,* Vol. 55, 1984, pp. 805–815.

7 Alpert, N. R., *Cardiac Hypertrophy,* Academic Press, New York, 1971.

8 Fung, Y. C., *Biodynamics: Circulation,* Springer-Verlag, New York, 1984.

9 Yin, F. C. P., "Ventricular Wall Stress," *Circ Res,* Vol. 49, 1981, pp. 829–842.

10 Yin, F. C. P., Strumpf, R. K., Chew, P. H., and Zeger, S. L., "Quantification of the Mechanical Properties of the Noncontracting Canine Myocardium Under Simultaneous Biaxial Loading," *J Biomech,* Vol. 20, 1987, pp. 577–589.

11 Fung, Y. C., *Biomechanics: Mechanical Properties of Living Tissues,* Spinger-Verlag, New York, 1981.

12 Omens, J. H., and Fung, Y. C., "Residual Strain in the Rat Left Ventricle," *Circ Res,* Vol. 66, 1990, pp. 37–45.

13 McCulloch, A. D., Smaill, B. H., and Hunter, P. J., "Regional Left Ventricular Epicardial Deformation in the Passive Dog Heart," *Circ Res,* Vol. 64, 1989, pp. 721–733.

14 Feit, T. S., "Diastolic Pressure-Volume Relations and Distribution of Pressure and Fiber Extension Across the Wall of a Model Left Ventricle," *Biophys, J.,* Vol. 28, 1979, pp. 143–166.

15 Tozeren, A., "Static Analysis of the Left Ventricle," ASME JOURNAL OF BIOMECHANICAL ENGINEERING, Vol. 105, 1983, pp. 39–46.

16 Arts, T., Reneman, R. S., and Veenstra, P. C., "A Model of the Mechanics of the Left Ventricle," *Ann Biomed Eng,* Vol. 7, 1979, pp. 299–318.

17 Humphrey, J. D., and Yin, F. C. P., "On Constitutive Relations and Finite Deformations of Passive Cardiac Tissue II: Stress Analysis in the Left Ventricle," *Circ Res,* Vol. 65, 1989, pp. 805–817.

18 Adkins, J. E., "Some General Results in the Theory of Large Elastic Deformations," *Proc R Soc, Series A,* Vol. 231, 1955, pp. 75–90.

19 Humphrey, J. D., Strumpf, R. K., and Yin, F. C. P., "A Theoretically-Based Experimental Approach for Identifying Vascular Constitutive Relations," *Biorheology,* Vol. 26, 1989, pp. 687–702.

20 Waldman, L.K., Fung, Y. C., and Covell, J. W., "Transmural Myocardial Deformation in the Canine Left Ventricle: Normal In Vivo Three-Dimensional Finite Strains," *Circ Res,* Vol. 57, 1985, pp. 152–163.

21 Spencer, A. J. M., *Continuum Mechanics,* Longman Press, 1980.

22 Vossoughi, J., Vaishnav, R. N., and Patel, D. J., "Compressibility of the Myocardial Tissue," *Adv Bioeng,* 1980, pp. 45–48.

23 Choung, C. J., and Fung, Y. C., "Residual Stress in Arteries," Schmid-Schonbein, G. W., Woo S. L.-Y., Zweifach, B. W., eds., *Frontiers in Biomechanics,* Springer-Verlag, New York, 1986, pp. 117–129.

24 Green, A. E., and Adkins, J. E., *Large Elastic Deformations and Non-Linear Continuum Mechanics,* Clarendon Press, Oxford, 1970.

25 The Numerical Algorithms Group Limited 1986.

26 Streeter, D. D. Jr., and Hanna, W. T., "Engineering Mechanics for Successive States in Canine Left Ventricular Myocardium: I. Cavity and Wall Geometry," *Circ Res,* Vol. 33, 1973, pp. 639–655.

27 Humphrey, J. D., and Yin, F. C. P., "On Constitutive Relations and Finite Deformations of Passive Cardiac Tissue: I. A Pseudostrain-Energy Function," ASME JOURNAL OF BIOMECHANICAL ENGINEERING, Vol. 109, 1987, pp. 298–304.

28 Caulfield, J. B., and Borg, T. K., "The Collagen Network of the Heart," *Lab Invest,* Vol. 40, 1979, pp. 364–372.

29 Waldman, L. K., Nosan, D., Villarreal, F., and Covell, J. W., "Relation Between Transmural Deformation and Local Myofiber Direction in Canine Left Ventricle," *Circ Res,* Vol. 63, 1988, pp. 550–562.

30 Nielsen, P. M. F., LeGrice, I. J., Smaill, B. H., and Hunter, P. J., "A Mathematical Model of the Geometry and Fibrous Structure of the Heart," *Am J Physiol,* 1991 (in press).

31 Gill, P. E., Murray, W., and Wright, M. H., *Practical Optimization,* Academic Press, New York, 1981, p. 351.

32 Grimm, A. F., Lin, H.-L., and Grimm, B. R., "Left Ventricular Free Wall and Intraventricular Pressure Sarcomere Length Distributions," *Am J Physiol,* Vol. 239, 1980, pp. H-101–H-107.

33 McCulloch, A. D., Smaill, B. H., and Hunter, P. J., "Left Ventricular

Epicardial Deformation in Isolated Arrested Dog Heart," *Am J Physiol,* Vol. 252, 1987, pp. H-233-H-241.

34 Villarreal, F. J., Waldman, L. K., and Lew, W. Y. W., "A Technique for Measuring Regional Two-Dimensional Finite Strains in the Canine Left Ventricle, *Circ Res,* Vol. 62, 1988, pp. 711-721.

35 Arts, T., Veenstra, P. C., and Reneman, R. S., "Epicardial Deformation and Left Ventricular Wall Mechanics During Ejection in the Dog," *Am J Physiol,* Vol. 243, 1982, pp. H-379-H-390.

36 Huisman, R. M., Elzinga, G., Westerhof, N., and Sipkema, P., "Measurement of Left Ventricular Wall Stress," *Cardiovasc Res,* Vol. 14, 1980, pp. 142-153.

37 Bergel, D. A., and Hunter, P. J., "The Mechanics of the Heart," Hwang, N. H. C., Gross, D. R., Patel, D. J., eds., *Quantitative Cardiovascular Studies,* University Park Press, Baltimore, 1979, pp. 151-213.

38 Mirsky, I., "Ventricular and Arterial Wall Stresses Based on Large Deformations Analyses," *Biophys J,* Vol. 13, 1973, pp. 1141-1157.

39 Demiray, H., "Stresses in Ventricular Wall," ASME *Journal of Applied Mechanics,* Vol. 43, 1976, pp. 194-197.

40 Abe, H., and Nakamura, T., "Finite Deformation Model for the Mechanical Behavior of Left Ventricular Wall Muscles," *Math Modeling,* Vol. 3, 1982, pp. 143-152.

41 Chadwick, R. S., "Mechanics of the Left Ventricle," *Biophys J,* Vol. 39, 1982, pp. 279-288.

42 Ritman, E. L., Heethaar, R. M., Robb, R. A., and Pao, Y. C., "Finite Element Analysis of Myocardial Diastolic Stress and Strain Relationships in the Intact Heart," *Eur J Cardiol,* Vol. 7, 1978, pp. 105-119.

43 Janz, R. F., Kubert, B. R., Moriarty, T. F., and Grimm, A. F., "Deformation of the Diastolic Left Ventricle: II. Nonlinear Geometric Effects," *J Biomech,* Vol. 7, 1974, pp. 509-516.

44 Pinto, J. G., and Fung, Y. C., "Mechanical Properties of the Heart Muscle in the Passive State," *J Biomech,* Vol. 6, 1973, pp. 597-616.

45 Kitabatake, A., and Suga, H., "Diastolic Stress-Strain Relation of Nonexcised Blood-Perfused Canine Papillary Muscle," *Am J Physiol,* Vol. 234, 1978, pp. H416-H420.

46 Pao, Y. C., Nagendra, G. K., Padiyan, R., and Ritman, E. L., "Derivation of Myocardial Fiber Stiffness Equation Based on the Theory of Laminated Composites," ASME Journal of Biomechanical Engineering, Vol. 102, 1980, pp. 252-257.

47 Humphrey, J. D., and Yin, F. C. P., "A New Constitutive Formulation for Characterizing the Mechanical Behavior of Soft Tissues," *Biophys J,* Vol. 52, 1987, pp. 563-570.

48 Horowitz, A., Lanir, Y., Yin, F. C. P., Perl, M., Sheinman, I., and Strumpf, R. K., "Structural Three-Dimensional Consitutive Law for the Passive Myocardium," ASME Journal of Biomechanical Engineering, Vol. 110, 1988, pp. 200-207.

49 Streeter, D. D. Jr., Spotnitz, H. M., Patel, D. P., Ross, J. Jr., and Sonnenblick, E. H., "Fiber Orientation in the Canine Left Ventricle During Diastole and Systole," *Circ Res,* Vol. 24, 1969, pp. 339-347.

50 Streeter, D. D., and Hanna, W. T., "Engineering Mechanics for Successive States in Canine Left Ventricular Myocardium: II. Fiber Angle and Sarcomere Length," *Circ Res,* Vol. 33, 1973, pp. 656-664.

51 Robinson, T. F., Cohen-Gould, L., and Factor, S. M., "Skeletal Framework of Mammalian Heart Muscle: Arrangement of Inter- and Pericellular Connective Tissue Structures," *Lab Invest,* Vol. 49, 1983, pp. 482-498.

52 Borg, T. K., Ranson, W. F., Moslehy, F. A., and Caulfield, J. B., "Structural Basis of Ventricular Stiffness," *Lab Invest,* Vol. 44, 1981, pp. 49-54.

53 Beyar, R., and Sideman, S., "Effect of the Twisting Motion on the Nonuniformities of Transmyocardial Fiber Mechanics and Energy Demand-A Theoretical Study," *IEEE Trans Biomed Eng,* Vol. 32, 1985, pp. 764-769.

54 Fung, Y. C., "Inversion of a Class of Nonlinear Stress-Strain Relationships of Biological Soft Tissue," ASME Journal of Biomechanical Engineering, Vol. 101, 1979, pp. 23-27.

55 Bogen, D. K., "Strain Energy Descriptions of Biological Swelling I: Single Fluid Compartment Models," ASME Journal of Biomechanical Engineering, Vol. 109, 1987, pp. 252-256.

56 Bogen, D. K., "Strain Energy Descriptions of Biological Swelling II: Multiple Fluid Compartment Models," ASME Journal of Biomechanical Engineering, Vol. 109, 1987, pp. 257-262.

APPENDIX 1

Substituting equation (13) into equation (12), one obtains full expressions for the stress components with respect to cylindrical polar coordinates:

$$T_{rr} = \left(\frac{R}{\lambda r}\right)^2 C(b_1 + b_3 \overline{E}_{RR})e^Q - p, \tag{A1a}$$

$$T_{\theta\theta} = \left(r\frac{d\phi}{dR}\right)^2 C(b_1 + b_3 \overline{E}_{RR})e^Q$$

$$+ \left[\frac{\alpha r}{R}\cos\Psi(R) + \beta r \sin\Psi(R)\right]^2 C(b_1 + b_2 \overline{E}_{FF})e^Q$$

$$+ \left[-\frac{\alpha r}{R}\sin\Psi(R) + \beta r \cos\Psi(R)\right]^2 C(b_1 + b_2 \overline{E}_{CC})e^Q$$

$$+ 2\left(r\frac{d\phi}{dR}\right)\left[\frac{\alpha r}{R}\cos\Psi(R) + \beta r \sin\Psi(R)\right]Cb_4 \overline{E}_{RF}e^Q$$

$$+ 2\left[\frac{\alpha r}{R}\cos\Psi(R) + \beta r \sin\Psi(R)\right]$$

$$\times \left[-\frac{\alpha r}{R}\sin\Psi(R) + \beta r \cos\Psi(R)\right]Cb_4 \overline{E}_{FC}e^Q$$

$$+ 2\left[-\frac{\alpha r}{R}\sin\Psi(R) + \beta r \cos\Psi(R)\right]$$

$$\times \left(r\frac{d\phi}{dR}\right)Cb_3 \overline{E}_{CR}e^Q - p, \tag{A1b}$$

$$T_{zz} = \left(\frac{d\omega}{dR}\right)^2 C(b_1 + b_3 \overline{E}_{RR})e^Q$$

$$+ \left[\frac{\gamma}{R}\cos\Psi(R) + \epsilon \sin\Psi(R)\right]^2 C(b_1 + b_2 \overline{E}_{FF})e^Q$$

$$+ \left[-\frac{\gamma}{R}\sin\Psi(R) + \epsilon \cos\Psi(R)\right]^2 C(b_1 + b_3 \overline{E}_{CC})e^Q$$

$$+ 2\left(\frac{d\omega}{dR}\right)\left[\frac{\gamma}{R}\cos\Psi(R) + \epsilon \sin\Psi(R)\right]Cb_4 \overline{E}_{RF}e^Q$$

$$+ 2\left[\frac{\gamma}{R}\cos\Psi(R) + \epsilon \sin\Psi(R)\right]\left[-\frac{\gamma}{R}\sin\Psi(R)\right.$$

$$\left. + \epsilon \cos\Psi(R)\right]Cb_4 \overline{E}_{FC}e^Q$$

$$+ 2\left[-\frac{\gamma}{R}\sin\Psi(R) + \epsilon \cos\Psi(R)\right]\left(\frac{d\omega}{dR}\right)Cb_3 \overline{E}_{CR}e^Q - p, \tag{A1c}$$

$$T_{r\theta} = \left(\frac{R}{\lambda r}\right)\left(r\frac{d\phi}{dR}\right)C(b_1 + b_3 \overline{E}_{RR})e^Q$$

$$+ \left(\frac{R}{\lambda r}\right)\left[\frac{\alpha r}{R}\cos\Psi(R) + \beta r \sin\Psi(R)\right]Cb_4 \overline{E}_{RF}e^Q$$

$$+ \left(\frac{R}{\lambda r}\right)\left[-\frac{\alpha r}{R}\sin\Psi(R) + \beta r \cos\Psi(R)\right]Cb_3 \overline{E}_{CR}e^Q, \tag{A1d}$$

$$T_{\theta z} = \left(r\frac{d\phi}{dR}\right)\left(\frac{d\omega}{dR}\right)C(b_1 + b_3 \overline{E}_{RR})e^Q$$

$$+ \left[\frac{\alpha r}{R}\cos\Psi(R) + \beta r \sin\Psi(R)\right]\left[\frac{\gamma}{R}\cos\Psi(R)\right.$$

$$\left. + \epsilon \sin\Psi(R)\right]C(b_1 + b_2 \overline{E}_{FF})e^Q$$

$$+ \left[-\frac{\alpha r}{R}\sin\Psi(R) + \beta r \cos\Psi(R)\right]\left[-\frac{\gamma}{R}\sin\Psi(R)\right.$$

$$\left. + \epsilon \cos\Psi(R)\right]C(b_1 + b_3 \overline{E}_{CC})e^Q$$

$$+ \left\{\left(r\frac{d\phi}{dR}\right)\left[\frac{\gamma}{R}\cos\Psi(R) + \epsilon \sin\Psi(R)\right] + \left[\frac{\alpha r}{R}\cos\Psi(R)\right.\right.$$

$$\left.\left. + \beta r \sin\Psi(R)\right]\left(\frac{d\omega}{dR}\right)\right\}Cb_4 \overline{E}_{RF}e^Q$$

$$+ \left[\frac{\alpha r}{R}\cos\Psi(R) + \beta r \sin\Psi(R)\right]\left[-\frac{\gamma}{R}\sin\Psi(R)\right.$$

$$+ \epsilon \cos\Psi(R) \Bigg] Cb_4 \overline{E}_{FC} e^Q$$

$$+ \left[-\frac{\alpha r}{R}\sin\Psi(R) + \beta r \cos\Psi(R) \right]\left[\frac{\gamma}{R}\cos\Psi(R) \right.$$

$$\left. + \epsilon \sin\Psi(R) \right] Cb_4 \overline{E}_{FC} e^Q$$

$$+ \left\{ \left[-\frac{\alpha r}{R}\sin\Psi(R) + \beta r \cos\Psi(R) \right]\left(\frac{d\omega}{dR} \right) \right.$$

$$\left. + \left(r\frac{d\phi}{dR} \right)\left[-\frac{\gamma}{R}\sin\Psi(R) + \epsilon\cos\Psi(R) \right] \right\} Cb_3 \overline{E}_{CR} e^Q, \quad (A1e)$$

$$T_{zr} = \left(\frac{R}{\lambda r} \right)\left(\frac{d\omega}{dR} \right) C(b_1 + b_3 \overline{E}_{RR}) e^Q$$

$$+ \left(\frac{R}{\lambda r} \right)\left[\frac{\gamma}{R}\cos\Psi(R) + \epsilon\sin\Psi(R) \right] Cb_4 \overline{E}_{RF} e^Q$$

$$+ \left(\frac{R}{\lambda r} \right)\left[-\frac{\gamma}{R}\sin\Psi(R) + \epsilon\cos\Psi(R) \right] Cb_3 \overline{E}_{CR} e^Q, \quad (A1f)$$

where (from equation (8))

$$\overline{E}_{RR} = E_{RR}, \quad (A2a)$$

$$\overline{E}_{FF} = E_{\Theta\Theta}\cos^2\Psi(R) + E_{ZZ}\sin^2\Psi(R) + 2E_{\Theta Z}\sin\Psi(R)\cos\Psi(R), \quad (A2b)$$

$$\overline{E}_{CC} = E_{ZZ}\cos^2\Psi(R) + E_{\Theta\Theta}\sin^2\Psi(R) - 2E_{\Theta Z}\sin\Psi(R)\cos\Psi(R), \quad (A2c)$$

$$\overline{E}_{RF} = E_{R\Theta}\cos\Psi(R) + E_{ZR}\sin\Psi(R), \quad (A2d)$$

$$\overline{E}_{FC} = E_{\Theta Z}[\cos^2\Psi(R) - \sin^2\Psi(R)]$$
$$+ (E_{ZZ} - E_{\Theta\Theta})\sin\Psi(R)\cos\Psi(R), \quad (A2e)$$

$$\overline{E}_{CR} = E_{ZR}\cos\Psi(R) - E_{R\Theta}\sin\Psi(R). \quad (A2f)$$

Similarly (from equation (18))

$$\overline{T}_{rr} = T_{rr}, \quad (A3a)$$

$$\overline{T}_{ff} = T_{\theta\theta}\cos^2\psi(r) + T_{zz}\sin^2\psi(r) + 2T_{\theta z}\sin\psi(r)\cos\psi(r), \quad (A3b)$$

$$\overline{T}_{cc} = T_{zz}\cos^2\psi(r) + T_{\theta\theta}\sin^2\psi(r) - 2T_{\theta z}\sin\psi(r)\cos\psi(r), \quad (A3c)$$

$$\overline{T}_{rf} = T_{r\theta}\cos\psi(r) + T_{zr}\sin\psi(r), \quad (A3d)$$

$$\overline{T}_{fc} = T_{\theta z}[\cos^2\psi(r) - \sin^2\psi(r)] + (T_{zz} - T_{\theta\theta})\sin\psi(r)\cos\psi(r), \quad (A3e)$$

$$\overline{T}_{cr} = T_{zr}\cos\psi(r) - T_{r\theta}\sin\psi(r). \quad (A3f)$$

APPENDIX 2

For a membrane subjected to a plane equibiaxial extension λ, the exponent Q in equation (13) and its derivative with respect to λ are

$$Q = b_1(2\lambda^2 + \lambda^{-4} - 3) + \frac{b_2}{4}(\lambda^2 - 1)^2 + \frac{b_3}{4}[(\lambda^{-4} - 1)^2 + (\lambda^2 - 1)^2]$$

and

$$\frac{dQ}{d\lambda} = 4b_1(\lambda - \lambda^{-5}) + (b_2 + b_3)(\lambda^3 - \lambda) + 2b_3(\lambda^{-5} - \lambda^{-9}).$$

Similarly, the fiber and cross-fiber stress components are (see Green and Adkins [24], p. 56)

$$\overline{T}_{ff} = C\left[b_1(\lambda^2 - \lambda^{-4}) + \frac{b_2}{2}(\lambda^4 - \lambda^2) + \frac{b_3}{2}(\lambda^{-4} - \lambda^{-8}) \right]e^Q$$

and

$$\overline{T}_{cc} = C\left[b_1(\lambda^2 - \lambda^{-4}) + \frac{b_3}{2}(\lambda^4 - \lambda^2 + \lambda^{-4} - \lambda^{-8}) \right]e^Q,$$

respectively. Finally, the material stiffness in the fiber and cross-fiber directions are obtained by taking derivatives of the respective stress component with respect to λ:

$$\frac{d\overline{T}_{ff}}{d\lambda} = C[b_1(2\lambda + 4\lambda^{-5}) + b_2(2\lambda^3 - \lambda)$$
$$+ b_3(4\lambda^{-9} - 2\lambda^{-5})]e^Q + \overline{T}_{ff}\frac{dQ}{d\lambda},$$

$$\frac{d\overline{T}_{cc}}{d\lambda} = C[b_1(2\lambda + 4\lambda^{-5}) + b_3(2\lambda^3 - \lambda + 4\lambda^{-9} - 2\lambda^{-5})]e^Q + \overline{T}_{ff}\frac{dQ}{d\lambda}.$$

f